

Amelia: A Large Dataset and Model for Airport Surface Movement Forecasting

Ingrid Navarro*, Pablo Ortega-Kral*, Jay Patrikar*, Haichuan Wang, Alonso Cano, Zelin Ye, Jong Hoon Park, Sebastian Scherer[†] and Jean Oh[†]
Carnegie Mellon University, Pittsburgh PA, USA, 15213

The growing demand for air travel necessitates advancements in air traffic management technologies to ensure safe and efficient operations. Predictive models for terminal airspace can help anticipate future movements and traffic flows, enabling proactive planning for efficient coordination, collision risk assessment, taxi-out time prediction, departure metering, and emission estimations. Although data-driven predictive models have shown promise in tackling some of these challenges, the absence of large-scale curated surface movement datasets in the public domain has hindered the development of scalable and generalizable approaches.

In this context, we propose the *Amelia* framework, which consists of four key contributions. First, *Amelia-48*, a large dataset of airport surface movement collected through the FAA's System Wide Information Management (SWIM) Program. This dataset includes over two years' worth of trajectory data (~70TB) across 48 US airports and map data. Second, we develop *Amelia-TF*, a large transformer-based baseline for multi-agent, multi-airport trajectory forecasting. Third, we propose *Amelia-10*, a training and evaluation benchmark consisting of 292 days of post-processed data from 10 different airports and a series of experiments to promote the development of foundation models in aviation. We provide baseline results across our benchmark using *Amelia-TF*. Finally, we release our framework and tools to encourage further aviation research in the forecasting domain and beyond at: ameliacmu.github.io

I. Introduction

WITHIN the first two months of 2023, the U.S. National Airspace System (NAS) recorded more aircraft close-calls than the total from the previous five years combined [1]. Poorly managed airport operations can have severe repercussions. For instance, in recent events, the world has experienced major incidents that have caused significant damage and, more importantly, resulted in the loss of human lives [2–4]. While some of these alarming trends can be, in part, traced back to deficiencies within the Air Traffic Control (ATC) facilities [5], the projected demands of the NAS indicate an increase in airspace capacity [6], which will further strain the existing infrastructure. For instance,

*Equal contribution

[†]Equal Advising

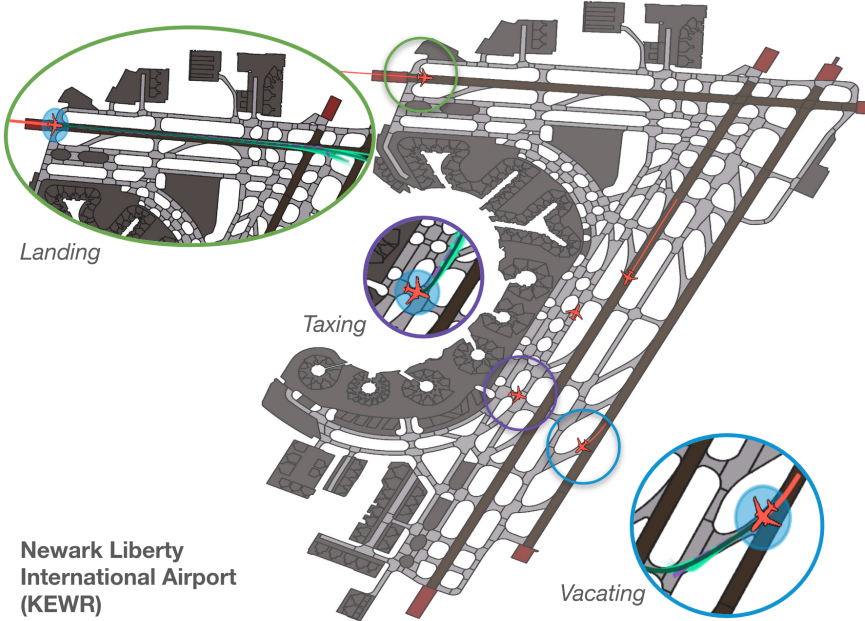


Fig. 1 An example of an **Amelia-48** scene showing various airport operations, e.g., landing (top-left), taxing (center), and vacating (bottom-right). The figure also shows **Amelia-TF**'s predicted trajectories (green segment) for each agent, given their trajectory histories (orange segment) and map information. Note: This paper is best read in color.

the year of 2023 set a record with the Transportation Security Administration (TSA) processing an astounding 2.9 million passengers in a single day [7]. Moreover, the development of Advanced Aerial Mobility (AAM) has seen a substantial increase in recent years, igniting interest in the creation of automated decision-support technologies that can be reliably integrated into the National Airspace System (NAS) to enable the concurrent use of airspace by both manned and unmanned aircraft [8].

The alarming frequency of incidents and the urgent challenges of incorporating AAM into human-centered airspace highlight a need for technological advancements in air traffic management and aviation safety standards. Developing effective strategies to understand and anticipate human interactions in this context is essential for identifying and mitigating potential failures that could result in catastrophic accidents.

In this context, data-driven human-aware predictive approaches, which have been widely successful in fields like autonomous driving [9–12] and crowd navigation [12–14], present significant potential to tackle these challenges. For instance, predictive models could be utilized by aircraft and management facilities to enhance airport safety, providing situational awareness through onboard sensors for intelligent navigation [15, 16] and automated go-around decisions to prevent near misses and collisions [17–20]. They could be utilized to improve airport management efficiency [21], for instance, by estimating taxi-out times and departure metering to coordinate pushbacks from the gate [22, 23], de-icing

schedules [24], and time-of-arrival estimates [25].

Although previous studies have tackled some of the challenges in airport surface operations, the absence of unified architectures and available open-source resources has limited the **generalizability and scalability** of these approaches [26]. Additionally, existing works in airport surface operations generally rely on small-scale datasets of a few airports [27, 28] or simple prediction models, such as straight-line prediction [29].

In response to this, this work contributes and open-sources the `Amelia` framework, a new dataset and a benchmark for airport safety. First, `Amelia-48` is a large-scale dataset focused on airport surface operations, which was collected through the Federal Aviation Administration’s (FAA) System Wide Information Management (SWIM) Program. `Amelia-48` includes trajectory data from 48 U.S. airports starting from December 1st of 2022 and currently boasts over 70TB of raw surface movement data. Alongside the SWIM data, we collect, post-process, and release airport surface maps as lightweight graphs with semantic markings for important attributes such as taxiways, runways, hold-short lines, etc. To the best of our knowledge, `Amelia-48` stands as the largest dataset of its kind and is geared towards use by researchers even beyond those interested in airport motion forecasting.

Next, we introduce `Amelia-10`, a scenario benchmark to encourage the development of large predictive models and general-purpose models for aviation. Our benchmark leverages a subset of our raw dataset, encompassing over 290 days of data for 10 different airports. `Amelia-10` consists of a family of experiments across two settings: `SingleAirport` and `MultiAirport`. The `SingleAirport` setting focuses on *within-domain* performance, i.e., training and testing model performance one airport at a time, while `MultiAirport` setting focuses on studying the generalization capabilities of predictive models under domain shifts.

Finally, to provide baseline results across our proposed benchmark, we contribute `Amelia-TF`, a large multi-modal, multi-agent trajectory forecasting model. `Amelia-TF` features a transformer-based [30] designed for predicting aircraft future movements by characterizing aircraft’s temporal information, agent-to-agent relationships, and airport geometry. `Amelia-TF` leverages a novel automated scene representation strategy that abstracts and prioritizes scene information to improve *within-domain* and *domain shift* model generalization. Using standard metrics for trajectory prediction, we provide both short- and long-horizon results across `Amelia-10`.

To promote further research in aviation, we release our framework and the tools utilized to build it and provide exhaustive documentation to encourage large-scale aviation research at: ameliacmu.github.io.

In summary, our contributions are the following:

- 1) We introduce `Amelia-48`, consisting of over 70TB of *raw* surface data from 48 U.S. airports. and
- 2) We introduce `Amelia-10`, a scenario benchmark to encourage the development of foundation models in aviation.
- 3) We introduce `Amelia-TF`, the first multi-modal, multi-agent airport surface movement forecasting model.
- 4) We release our framework to propel large-scale open-source aviation research.

II. Related Work

A. Trajectory Forecasting Datasets

In contrast to the autonomous driving (AD) domain, where large-scale datasets exist [9–12], the domain of aviation has not been studied as extensively due in part to the lack of datasets. Previous works [26] have criticized the dominance of proprietary, non-public data in aviation research, finding that 68% of the works reviewed utilized solely proprietary data. In response, *TrajAir* [31] was introduced as a multi-modal dataset in the public domain for motion prediction in general aviation. *TrajAir* aimed to learn how pilots interact in non-towered airports but focused only on one airport. Accordingly, in response to the lack of curated large-scale publicly accessible datasets in this domain, we release the *Amelia-48* dataset. To the best of our knowledge, *Amelia-48* is the largest dataset of its kind and is geared towards use by researchers even beyond those interested in airport motion forecasting.

B. Trajectory Forecasting Models

The field of data-driven trajectory prediction aims to characterize and reason over human interactions leveraging complex temporal, interactive, and contextual relationships within the data. Modeling techniques have been widely explored within the domains of autonomous driving [32–37] and motion in human crowds [12, 36, 38–40].

Finally, as highlighted in [41], existing AD datasets often rely on surface-level metrics encompassing traffic crowdedness and motion complexity to mine for interesting scenarios and select agents *to predict* [9–11]. Similar to [41], we believe that leveraging these metrics alone to select interactions of interest may overlook more subtle, safety-relevant interactive behavior, which is especially important in domains where safety is critical. As such, as part of our modeling strategy, we propose a novel scenario representation approach that leverages a safety-informed scoring methodology to select and encode agents of interest in a given airport surface scene.

C. Trajectory Forecasting in Aviation

Motivated by the growing challenges of coordinating air traffic, an emerging research area focuses on employing learning-based trajectory forecasting to the aviation domain. The bulk of prior art [42–44] has mainly focused on short-term in-air trajectory prediction. Among the first to do so is FlightBERT [42], which introduces a novel binarized encoding for each trajectory point, framing forecasting as a multi-binary classification problem. Concretely each trajectory point -consisting of latitude, longitude, altitude and speed- is represented as binary string rather than a scalar before being projected into a latent space by a trajectory encoder which employs attention to capture dependencies between the attributes of the trajectory; the resulting embeddings are then fed into a transformer-based network and finally to a prediction head, which is a fully connected layer followed by a sigmoid function that projects the enriched embeddings into a prediction vector.

Closest to our work is [27], which also proposes prediction models characterizing airport surface movement

operations. In this work, the authors leverage the FAA’s SWIM information system to analyze four hours’ worth of movement at two airports, identifying the 2D position of each agent and state described in terms of acceleration and velocity as attributes of interest. Another work [45] uses one-week ADS-B data collected at Singapore Changi Airport. While these works do not release the data in the public domain, a significant drawback is the lack of generalizability to other airports due to a limited scope and scale

Our work differs significantly in scale and scope, as we wish to forecast trajectories for airport ground operations across multiple airport topologies. This necessitates three main key points that current approaches forgo:

- 1) **Interaction Modeling** Approaches such as FlightBERT are fundamentally not designed for modeling social behaviors, as the core idea is to better learn single trajectory dynamics by projecting trajectory features into a higher dimensionality; this becomes intractable when analyzing scenes where multiple agents are interacting.
- 2) **Context Awareness** Our application domain, ground operations, requires modeling contextual information that captures the movement zones that condition different behaviors.
- 3) **Efficient Scene Encoding** The scale of our dataset presents a challenge regarding efficiently processing the data in a computationally feasible manner and favors generalization. FlightBERT uses absolute trajectory representations, which could increase the sample complexity of the data points and hinder generalization to out-of-distribution cases.

III. The Amelia-48 Dataset

Surface area operations refer to aircraft and vehicle movements on or near the airport surface. In this study, we focus on defining surface movements to include aircraft landing, taking off, and taxiing within the designated airport movement area, as well as vehicle movements. We are interested in predicting agent behavior within this area; therefore, we aim to capture any aircraft and vehicle trajectory that enters it. The scope ends when the agent either exits the area or crosses the non-movement boundary markings on the airport surface. To use the collected data for training a trajectory forecasting model, we transform the raw position reports into smooth trajectories that include agent metadata. The processed data format is compatible with existing dataloaders for motion forecasting [37]. We detail our collection and processing methodologies for the trajectory data in Section III.A and map data Section III.B.

A. Trajectory Data

To build Amelia-48, we leverage the System Wide Information Management (SWIM) Program [46], an information system that provides a repository of aviation data spanning the National Airspace System. We utilize the SWIM Terminal Data Distribution System (STDDS), which aggregates terminal data from various sources like Airport Surface Detection Equipment – Model X (ADSE-X), and Airport Surface Surveillance Capability into a single data stream providing position reports for aircraft and vehicles operating within a few miles of the airport, covering *approaching*

and *ground movement* events. The raw dataset is a collection of SMES messages covering Terminal Radar Approach Control Facilities (TRACONs) within the NAS. Our data collection started on December 1st, 2022, and represents **over 70TB** of raw trajectory data recorded and stored on our in-house server. We ensure redundancy against server downtime and networking snags in our collection process through concurrent Advanced Message Queuing Protocol [47] connections. Each connection records data for one hour and then offloads the data to storage as a tarball.

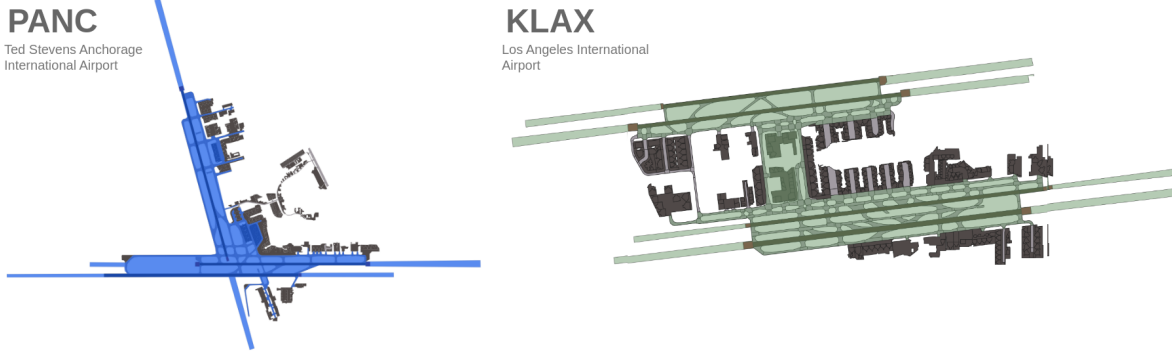


Fig. 2 Examples of polygonal fences used for collecting position reports within the airports' movement areas.

To process the raw position messages, we further develop data pre-processing scripts following [31]. Here, we focus on 48 airports in the US*, for which we produce clean interpolated data in formats suitable for most modern ML-based trajectory forecasting dataloaders. We do so by defining a 3D geographical fence around the airport of interest, as shown in Figure 2, and then filtering the position reports that fall inside it and within 2000ft above ground level.

We also extract relevant metadata from each position report which we then interpolate and resample at 1Hz. We produce CSV files corresponding to one hour of data for each airport. Table 1 shows the various fields in each CSV with their units and descriptions. To get the local cartesian coordinates, we pick an arbitrary origin within the airport surface.

B. Map Data

We use OpenStreetMap (OSM) [48] and OSMNx [49] to collect and produce surface maps for the airports in Amelia-48. Raw OSM airport maps are dense routing graphs containing centerline information of the movement areas, pavement boundaries, and semantic information, e.g., taxiways, runways, hold-short lines, exit lines, aprons, etc. As an example, Figure 3.a) shows a small region of the *Seattle-Tacoma Airport* in its raw representation. Node elements within the graph contain geographical coordinates (latitude, longitude) and local Cartesian coordinates, (x, y) , expressed w.r.t. an arbitrary origin.

To obtain a more compact representation of the map, thereon, apply a series of automated steps to only maintain elements of interest. We begin by filtering the graph such that only edges and nodes pertaining to centerlines of movement areas are maintained. These are then classified into the following semantic classes: runway, taxiway, and

*List of currently supported airports: ameliacmu.github.io/amelia-dataset/.

Table 1 List of fields with corresponding units and descriptions in the pre-processed **Amelia-48** dataset.

Field	Units	Description
Frame	#	Timestamp
ID	#	STDSS Agent ID
Altitude	feet	Agent Altitude (Mean Sea Level)
Range	km	Distance from airport datum
Bearing	rads	Bearing Angle w.r.t. North
Lat	decimal degs	Latitude of the agent
Lon	decimal degs	Longitude of the agent
Speed	knots	Agent Speed
Heading	degrees	Agent Heading
x	km	Local X Cartesian Position
y	km	Local Y Cartesian Position
Type	int	Agent Type [0:aircraft, 1:vehicle, 2:unknown]
Interp	boolean	Interpolated data point flag

hold-lines, which indicate the exit boundary of runway-protected areas (Figure 3.b). We then extend runway endpoints by a nautical mile to encompass landing and take-off procedures (Figure 3.c). Lastly, we super-sample the runway centerlines to obtain a finer runway representation (Figure 3.d).

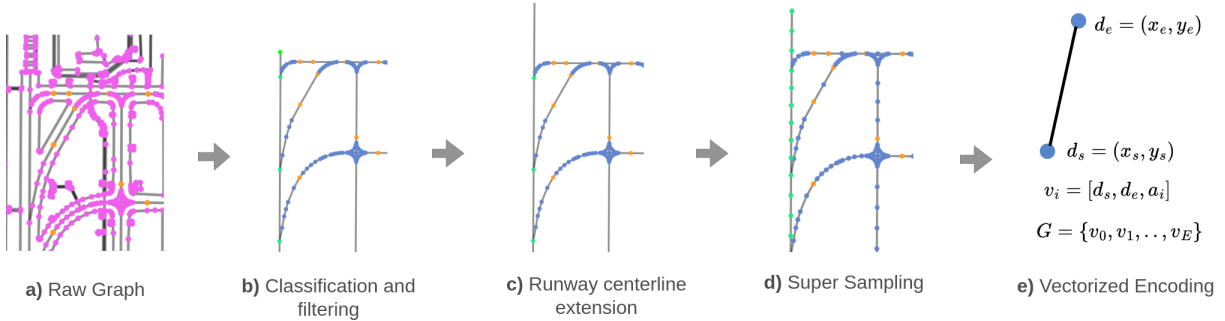


Fig. 3 Overview of our automated map processing pipeline which converts raw maps from OpenStreetMap into compact, easy-to-use semantic airport graphs.

Finally, following [32], we encode the graph in a vectorized manner (Figure 3.e), where an edge i is described as a vector, $v_i = [d_i^s, d_i^e, a_i]$, with $d_i^s \in \mathbb{R}^{1 \times 4}$ and $d_i^e \in \mathbb{R}^{1 \times 4}$ being the start and end nodes containing the geographical and relative coordinates, and $a_i \in \mathbb{N}^{1 \times 3}$ a one-hot encoded vector indicating one of semantic classes.

IV. The **Amelia-10** Benchmark

The **Amelia-10** is a scenario benchmark aimed at studying the generalization capabilities of predictive models through a family of *within-domain* and *domain-shift* experiments. The benchmark data consists of a subset of the **Amelia-48**, consisting of 10 different airports over the span of 292 days. These airports were selected to ensure diversity across airport topologies and crowdedness levels. We provide a validation analysis of the selected airports in

Section IV.A and details of the benchmark design in Section IV.B.

A. The Amelia-10 Dataset Analysis and Validation

1. Trajectory Data

Our selected airports are shown in Figure 4 along with their names and International Civil Aviation Organization (ICAO) identifiers, which we use for brevity throughout the paper. We process one month’s worth of data for each selected airport, totaling 292 days. Figure 4 shows processed trajectories overlaid on top of their corresponding map. We maintain the figure’s color coding for each airport throughout the paper. The trajectories span beyond the runway limits to allow capturing landing and take-off rolls. The figure also shows each airport’s *crowdedness* (y-axis) *per-hour-of-day* (x-axis), with a solid line showing the maximum recorded agent density. The plots validate that our selected airports widely vary in traffic density and variance across hours. For instance **KMSY**, **PANC** and **KMDW** are significantly less crowded than **KJFK** and **KLAX**.

Table 2 further supports this, providing a quantitative summary of each airport’s traffic information including the *total* and *per-category* number of unique agents and unique data points. The table includes additional information such as the month from which we sampled the data, and data quality in terms of interpolated points and agent type percentages (Interp and Type in Table 1). For instance, out of the ~300M global data points, only 3.46% of the data points were interpolated, suggesting minimal need for interpolation. Finally, while we note that the majority of the unique agents (~83.47%) are classified as *unknown*, we have no control over the agent categorization process, and improvements to such process are out of the scope of our work.

Table 2 Raw trajectory data summary per airport showing the *total* and *per-category* number of unique agents and data points along with the percentage of interpolated points.

Airport	Month	Total		Aircraft		Vehicles		Unknown	
		Num. Agents	Num. Data Points (% Interp.)	Num. Agents (% w.r.t. Total)	Num. Data Points (% Interp.)	Num. Agents (% w.r.t. Total)	Num. Data Points (% Interp.)	Num. Agents (% w.r.t. Total)	Num. Data Points (% Interp.)
PANC	Nov	131.35k	15.43M (0.22%)	16.96k (12.91%)	5.88M (0.15%)	4.01k (3.12%)	2.51M (0.84%)	110.29k (83.97%)	7.035M (0.06%)
KBOS	Jan	94.99k	23.39M (0.62%)	33.44k (35.20%)	14.77M (0.45%)	4.27k (4.50%)	2.94M (1.33%)	57.29k (60.30%)	5.68M (0.68%)
KEWR	Mar	140.81k	30.86M (4.86%)	38.86k (27.59%)	20.81M (5.67%)	2.21k (1.57%)	1.23M (8.32%)	99.75k (70.84%)	8.81M (2.47%)
KDCA	Dec	61.85k	17.78M (9.94%)	25.81k (41.73%)	8.22M (8.29%)	1.30k (2.10%)	1.00M (16.82%)	34.74k (56.17%)	8.56M (10.72%)
KJFK	Apr	645.41k	52.82M (9.89%)	45.15k (6.99%)	28.02M (12.03%)	156 (0.02%)	66.31k (4.66%)	600.11k (92.98%)	24.73M (7.47%)
KLAX	May	451.80k	42.81M (0.49%)	60.24k (13.33%)	24.67M (0.30%)	14.92k (3.30%)	2.79M (3.33%)	376.70k (83.38%)	15.35M (0.27%)
KMDW	Jun	211.92k	28.51M (0.84%)	22.47k (10.61%)	6.69M (0.32%)	6.28k (2.97%)	6.15M (3.35%)	183.22k (86.46%)	15.67M (0.07%)
KMSY	Jul	49.35k	10.37M (0.13%)	10.42k (21.12%)	2.57M (0.08%)	54 (0.11%)	39.89k (3.07%)	38.87k (78.77%)	7.75M (0.13%)
KSEA	Aug	378.54k	38.48M (0.23%)	50.08k (13.23%)	26.13M (0.19%)	290 (0.08%)	274.94k (1.02%)	328.17k (86.70%)	12.077M (0.31%)
KSFO	Sep	185.87k	36.01M (2.91%)	37.36k (20.10%)	16.67M (2.84%)	14.57k (7.84%)	5.65M (3.26%)	133.94k (72.06%)	13.69M (2.87%)
Total		2,351,883	296,448,313 (3.46%)	340,791 (14.49%)	154,436,226 (3.84%)	48,149 (2.05%)	22,653,655 (3.63%)	1,963,086 (83.47%)	119,354,023 (2.95%)

Finally, we validate aircraft motion profiles across airports in Figure 5. Specifically, we focus on (1) heading change in subsequent timesteps, (2) mean speed and (3) mean acceleration per trajectory. We see that speed and heading have an ample spread, reflecting the different aircraft behaviors, e.g., take-off taxiing, vacating, etc. The acceleration profile shows a majority of stationary sequences (0 m/s^2 bin), which aligns with the behavior of stationary aircraft awaiting

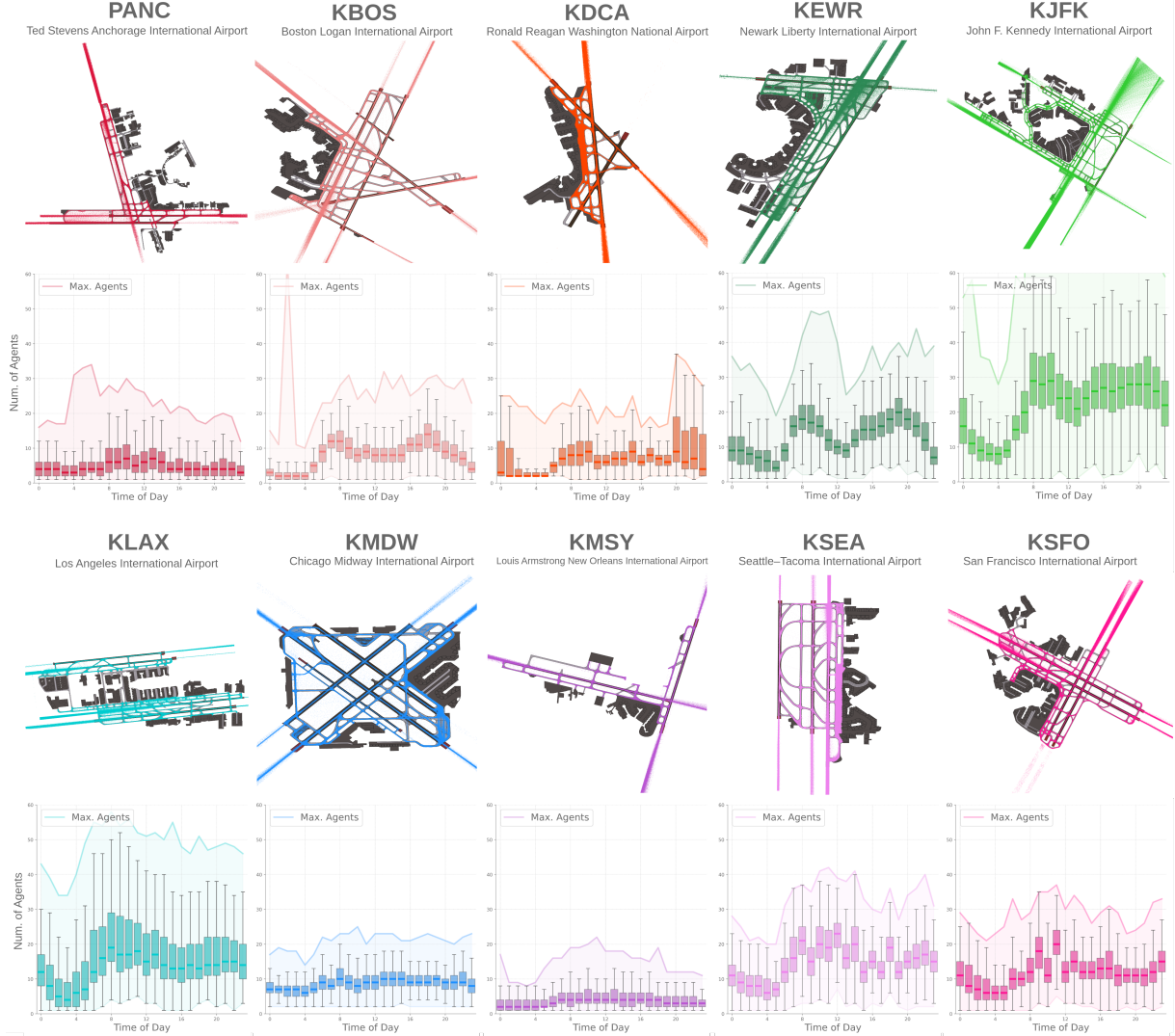


Fig. 4 Overview of the processed airport trajectory data. We study 10 airports with varying crowdedness and map topologies. For each airport, we overlay a month’s worth of processed trajectories spanning beyond runway limits to capture landing and take-off rolls. We also show each airport’s crowdedness per hour-of-day.

clearance or gate assignment, while the noticeable high deceleration and acceleration profiles correspond to aircraft landing and taking off. While diverse across airports, the speed, acceleration, and heading change follow a similar trend, indicating consistent aircraft behavior and verifying that *Amelia-48* accurately captures desired ground operation behaviors.

2. Map Data Analysis

Table 3 shows that our selected airports also vary at the topological level. First, our selection includes airports with different runway configurations, e.g., *parallel* (P) and *interesecting* (I) runways, and also considering complex topologies which include various combinations of *both* (B) types. We also summarize each airport’s graph. We show

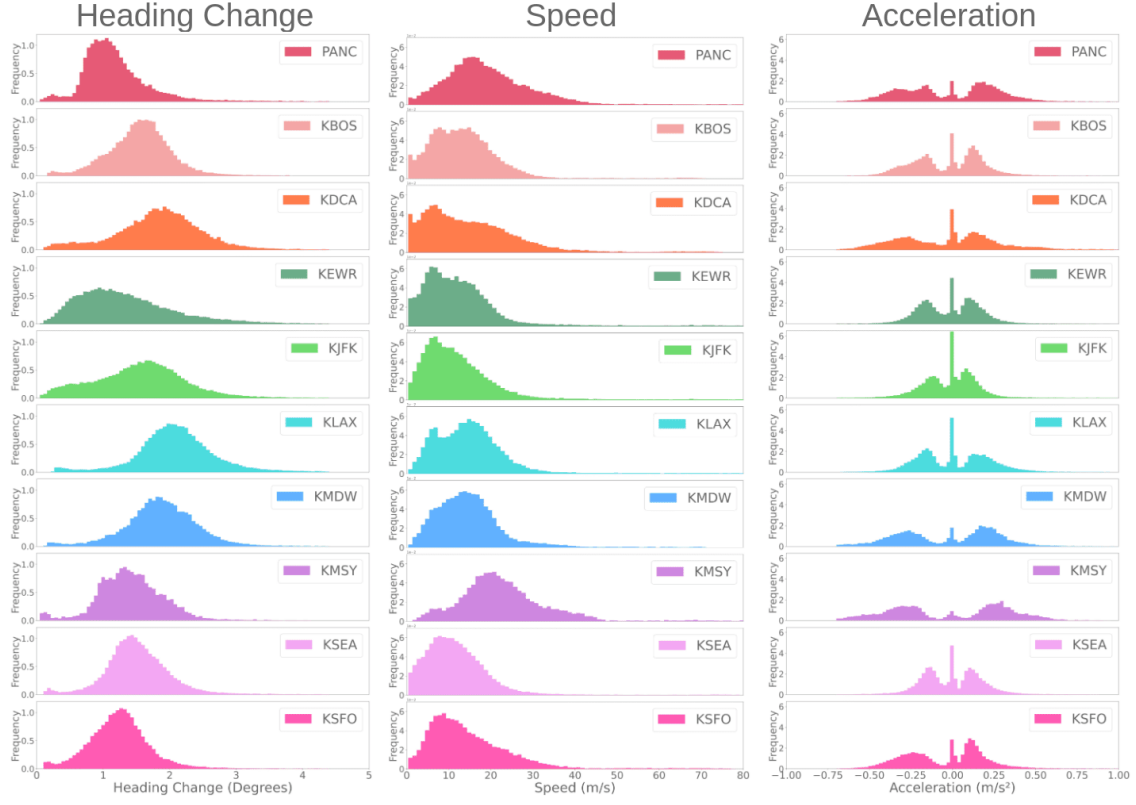


Fig. 5 Aircraft motion profiles per airport. The first column shows the mean heading change per timestep. The second and third columns show the mean speed and acceleration per trajectory. All plots are shown as probability densities.

the *total* and *per-category* number of nodes in each graph. From these numbers, we can contrast the relative complexity between maps, e.g., a *low*-complexity map such as KMSY which only has $\sim 1.5k$ nodes vs. a *high*-complexity one like KLAX with $\sim 11k$.

Table 3 Map data summary per airport showing runway count and topology, *total* and *per-category* node count.

Airport	Num. Runways	Runway Topology	Graph Nodes			
			Total	Runway	Taxiways	Hold Line
PANC	3	C	8,016	676	7,134	206
KBOS	5	C	5,056	944	3,826	286
KDCA	3	I	8,154	438	7,590	126
KEWR	3	C	4,804	1,424	3,090	290
KJFK	4	C	7,090	762	5,820	508
KLAX	4	P	10,728	766	9,224	738
KMDW	5	C	4,132	582	3,122	428
KMSY	2	I	1,408	474	790	144
KSEA	3	P	4,782	540	4,000	242
KSFO	4	C	9,032	686	7,992	354

P: parallel, I: intersecting, C: combined topology, i.e., parallel and intersecting runways.

B. The **Amelia-10** Experiment Family

The benchmark consists of two settings: `SingleAirport` and `MultiAirport`. In `SingleAirport`, we focus on assessing *within-domain* performance by training and testing our model’s performance one airport at a time. This setting, therefore, consists of 10 experiments, one per environment.

To find a middle ground between scale and generalizability, our benchmark also aims to investigate the performance of predictive models under *domain shifts*. Therefore, we propose a sweep of `MultiAirport` experiments aimed at evaluating generalization performance as we increasingly constrain training environments. The sweep consists of 6 experiments: 10-Seen, 7-Seen, 4-Seen, 3-Seen, 2-Seen, and 1-Seen, each named according to the number of training airports. The experiments with a greater number of *seen* airports are supersets of those with a smaller number.

We consider topological diversity and the crowdedness scale to determine the `MultiAirport` order. For topological diversity, we focus on the runway organization (see Table 3), and we use the number of unique data points as a proxy for the crowdedness scale level (see Table 2). In the list below, we summarize the selection per experiment, i.e., the airports that get removed from the training set. In parenthesis, we include the airport’s runway topology (P: parallel, I: intersecting, and C: combined) and scale rank from 1 (lowest) to 10 (highest).

- 10-Seen: We include all airports, i.e., all topology types and scales. Here, 6 airports have combined topologies, 2 intersecting runways only, and 2 parallel runways only.
- 7-Seen: We remove one airport per topology type from 10-Seen: KLAX (P, 9), KMSY (I, 1), KJFK (C, 10).
- 4-Seen: We remove one airport per topology type from 7-Seen: KSEA (P, 8), KDCA (I, 3), PANC (C, 2). All of the remaining airports have combined topology and a variety of scales to ensure interaction diversity.
- 3-Seen: We remove the largest-scale airport from 4-Seen, KSFO (C, 7).
- 2-Seen: We remove the smallest-scale airport from 3-Seen, KBOS (C, 4).
- 1-Seen: We remove the largest-scale airport from 2-Seen, KEWR (C, 6). The only seen airport is KMDW (C, 5).

Finally, the objective of this benchmark is to minimize the zero-shot performance drop between *within-domain* and *domain-shift* performance and ultimately to bridge the gap between `SingleAirport` and `MultiAirport`.

V. The **Amelia** Trajectory Forecasting (**Amelia-TF**) Model

To provide baseline results for the **Amelia-10** benchmark, we introduce **Amelia-TF**, an end-to-end trajectory forecasting model that aims to characterize *relevant* surface area operations as those described in Section III. To achieve this, we build upon the intuitions from prominent state-of-the-art models to design a model capable of learning strong feature representations [35, 37], as well as automated methods for selecting relevant scenes and agents to characterize [41]. Our model comprises three main submodules: (1) a **scene representation** module that determines the agents of interest in the scene and encodes per-agent features; (2) a transformer-based **scene encoder** [33, 37, 50], which hierarchically encodes the *temporal*, *agent-to-agent* and *agent-to-context* relationships within a scene, and; (3) a

Amelia-TF

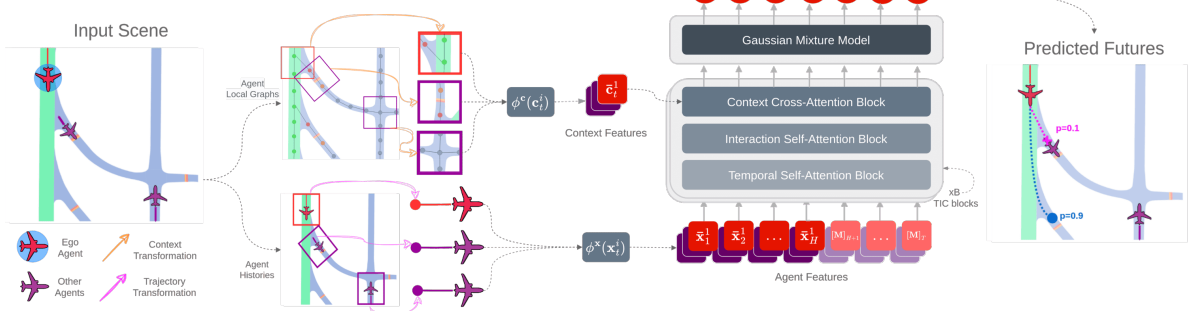


Fig. 6 Overview of Amelia-TF. For a given scene, Amelia-TF takes agent trajectories and their corresponding local context graphs as modalities of information and transforms them w.r.t. a pre-selected *ego-agent*. It then encodes the scene via blocks of transformer layers that attend over *temporal* and *agent-to-agent*, and *agent-to-context* relationships within a scene. Finally, the resulting feature is fed to a Gaussian Mixture Model which produces a distribution over the possible agent futures.

trajectory decoder that models the set of possible futures with associated confidence scores using a Gaussian Mixture Model. An overview of the model is shown in Figure 6, and formulation and model details are described below.

A. Problem Formulation

1. Notation Details

We define $\mathbf{x}_t^i \in \mathbb{R}^D$ as the state of an agent i at some timestep t . In this work, a state represents an agent's 3D coordinates and heading, i.e., $\mathbf{x}_t^i = (x, y, z, \theta)_t^i$. We represent a trajectory as a sequence of states from some timestep t_m to another timestep t_n as $\mathbf{x}_{t_m:t_n}^i$. Next, to represent a feature and a prediction we use the bar, e.g., $\bar{\mathbf{x}}$, and hat, e.g., $\hat{\mathbf{x}}$, respectively. We use parentheses for the superscripts to refer to a layer number, e.g., $\bar{\mathbf{x}}^{(l)}$, represents a state feature at layer l . Finally, we omit superscripts to refer to joint representations, e.g., $\mathbf{x}_t = [\mathbf{x}_t^1, \dots, \mathbf{x}_t^N] \in \mathbb{R}^{N \times D}$, is the joint state for all agents in a scene.

Along with agent poses, we leverage semantic graph representations, as those delineated in Section III.B, to further contextualize each agent's state. We define this context as $\mathbf{c}_t^i \in \mathbb{R}^{P \times C}$, where P is the number of nodes making up the graph, and C is the dimensionality of a node. We follow the same notation details to represent the context of an agent, \mathbf{c}_t^i , a trajectory of contexts, $\mathbf{c}_{t_m:t_n}^i$, and a joint context, \mathbf{c}_t . In general, context can be shared among all agents in the scene, or local for each agent in the scene. As we will detail in Section V.B, we use a local context representation for each agent, which we interchangeably refer to as local patches.

2. Problem Statement

We define a scene as the joint set of K agent sequences in the environment of interest, along with their corresponding context information. The scene has a total length of T seconds, where agents whose trajectories are shorter (e.g., agents that exit the scene earlier, or enter it later) are padded with zeroes. Each trajectory is then split into an observation and a

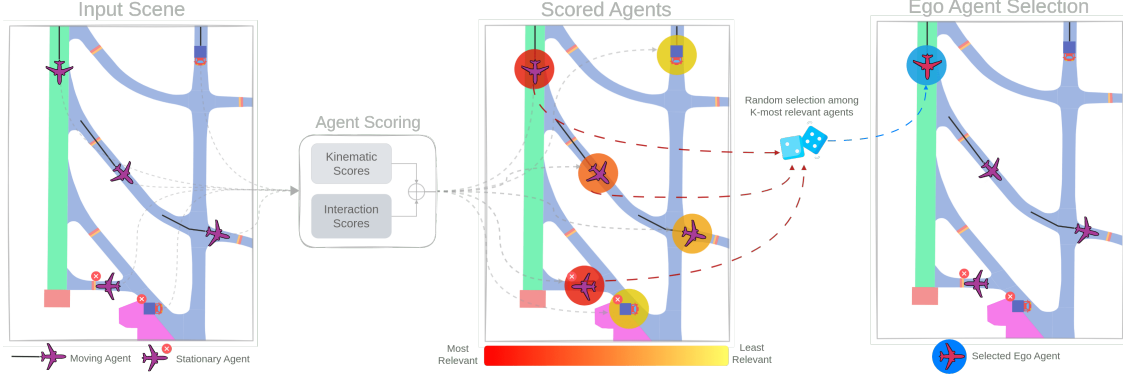


Fig. 7 Overview of our scene representation methodology. Given an input scene consisting of N agents, we compute a score for each agent representing its *kinematic* and *interactive* profile. To represent the final scene, we keep the K -most relevant, as deemed by the scoring function. Finally, the ego-agent is randomly selected among the K -agents.

prediction segment. The observed portion is defined as $\mathbf{x}_{t_o-H:t_o}^i$, where t_o is the last observed timestep, and H is the length of the agent’s observed history. Similarly, to represent the future horizon we use $\mathbf{x}_{t_p:t_p+F}^i$, where t_p is the first future time step and F is the length of the future segment. Each trajectory has a context history, $\mathbf{c}_{t_o-H:t_o}^i$.

For an agent i , the goal of a trajectory forecasting model is to learn a distribution of M possible future trajectories given the agents’ observed history,

$$\hat{\mathbf{x}}_{m, t_p:t_p+F}^i \sim P_{\theta}(\cdot | \mathbf{x}_{t_o-H:t_o}^i, \mathbf{c}_{t_o-H:t_o}^i) \quad \forall m \in \{1, \dots, M\}$$

where θ represents the learned parameters of the model.

B. Scene Representation

We follow an ego-centric scene representation where all agent trajectories and contexts in a scene are encoded w.r.t. to a pre-selected agent, known here as *ego-agent*.

We aim to characterize *safety-relevant* behaviors and interactions within airport operations such as aircraft preparing for take-off, stationary aircraft near hold-short lines, aircraft landing and taxiing out. Raw scenes, however, may contain non-critical agents, such as stationary agents in low-conflict regions. Consequently, the learned model may only be able to predict trivial cases. Thus, to encourage *Amelia* to focus on more complex and critical behavior, we build a novel selection method inspired by prior work [41], for both, selecting relevant ego-agents and producing complex scene representations.

An overview and toy example of our scene representation and ego-agent selection methodology is shown in Figure 7. The example depicts an airport scene with a variety of behaviors: an aircraft landing on a **runway**, two aircraft vacating a **taxiway**, an aircraft waiting near a **hold-short line**, and two vehicles. To select the most relevant agents, our method

takes each agent’s trajectory and map information and computes a score indicating how *critical* it is; where the higher the score, the more critical the agent is deemed. Our score, specifically, is the result of a function describing a proxy for the agent’s *kinematic* and *interaction* states as in [41].

For the **kinematic** state, we encode the agent’s speed, acceleration, and jerk profiles. We further account for stationary and slow-moving agents near hold-short lines, which are regions where an aircraft should stop before entering a runway. These are especially important since they help ensure an aircraft’s proper positioning. To characterize these situations we, thus, incorporate a waiting interval measure weighted by the inverse of the distance to the hold line. For the **interaction** state, we consider each agent pair and measure their loss of separation value as in [15], as well as a measure indicating the minimum time to conflict point between the agents’ trajectories and conflict regions in the map.

Once each agent is scored, we select the K -most critical agents to represent the final scene. Next, we randomly choose the ego-agent, e , among the selected agents and transform the scene w.r.t. its pose at the last observed timestep, $\mathbf{x}_{t_o}^e$. The final transformed trajectories, $\mathbf{x}_{t_o-H:t_o} \in \mathbb{R}^{K \times H \times D}$, are encoded as,

$$\bar{\mathbf{x}}_{t_o-H:t_o} = \phi^{\mathbf{x}}(\mathbf{x}_{t_o-H:t_o}) + \text{PE}(\mathbf{x}_{t_o-H:t_o})$$

where $\phi^{\mathbf{x}}$ is an MLP and PE is a positional embedding.

Similarly, we encode the transformed context graphs, $\mathbf{c}_{t_o-H:t_o} \in \mathbb{R}^{K \times H \times P \times C}$ as,

$$\bar{\mathbf{c}}_{t_o-H:t_o} = \phi^{\mathbf{c}}(\mathbf{c}_{t_o-H:t_o})$$

where $\phi^{\mathbf{c}}$ is a map feature extractor based upon *VectorNet* [32]. Note that our model encodes individual local patches for each agent in the scene, in contrast to prior works where a shared global context is used for all agents in the scene [32, 35, 37]. The intuition behind it is that, in aviation, relevant interactions are not necessarily local as would often be the case for settings such as autonomous driving or navigation in human crowds. For instance, while an autonomous vehicle might be more interested in potential interactions with vehicles at a nearby intersection or conflict region, an aircraft might be interested in the potential interaction with an agent at the other end of the runway. In our domain, however, encoding the global airport map information in the scene may make it difficult for the model to generalize to unseen settings. Thus, we opt for a local context encoding and assume that relative distances between agents and context regions are preserved in the ego-centric scene transformation.

C. Scene Encoder

Our trajectory forecasting model follows a transformer-based architecture that uses a factorized attention scheme for efficient computations as in [37]. The model maintains a $K \times F \times D$ representation across all transformer layers while

interleaving two types of self-attention layers: a *temporal* and an *interaction* one, as well as a *context* cross-attention layer as shown in Figure 6. For brevity, we refer to a block comprising these three layers subsequently as TIC.

The **temporal** layer is designed as a causal transformer [50] used for learning the time-wise dependencies within trajectories. It does so by attending to past features across the time dimension using a mask operator, \mathbf{M} , that only *looks* at the previous states from a given timestep. Then, the **interaction** layer is designed to learn agent-to-agent relationships by attending over the features across the agent dimension. We implement both of these layers as multi-head attention (MHA) blocks [30] which receive the joint feature from the previous layer, $\bar{\mathbf{x}}^{(l-1)}$, as the query, key, and value parameters, producing a feature $\bar{\mathbf{x}}^{(l)}$. The **context** cross-attention layer is then used to exploit the relationships between agent and map features. This layer is also implemented as a MHA block, however, using agents' joint feature as the query input, while the keys and values are obtained from the embedded context.

Our scene encoder consists of multiple TIC blocks, stacked sequentially to obtain a richer representation (Section VI). For details on the intuitions and benefits of using factorized attention mechanisms, we refer the reader to [37, 51].

D. Trajectory Decoder

To model the distribution of possible futures for a scene, we adopt a Gaussian Mixture Model (GMM) as [35, 52] which can be formulated as a weighted sum over the mixture,

$$p(\mathbf{x}) = \sum_{m=1}^M \rho_m \cdot \mathcal{N}_m(\mathbf{x} - \boldsymbol{\mu}_x, \boldsymbol{\Sigma}_x)$$

where each mode, m , is conditionally independent over timesteps, producing a distribution \mathcal{N}_m with mean $\boldsymbol{\mu}_x \in \mathbb{R}^D$ and covariance $\boldsymbol{\Sigma}_x \in \mathbb{R}^{D \times D}$ over \mathbf{x} . Each mode has a tied weight, ρ_m , representing its likelihood over time, where $\sum_{m=1}^M \rho_m = 1$. We model the GMM as an neural network that receives the output feature at the final layer, L , of the scene encoder,

$$\bar{\mathbf{z}}_{t_p+F:t_p} = \phi^{gmm}(\bar{\mathbf{x}}_{t_o-H:t_o}^{(L)})$$

producing a feature, $\bar{\mathbf{z}} \in \mathbb{R}^{K \times M \times F \times 7}$, following the format $(\mu_x, \mu_y, \mu_z, \sigma_x, \sigma_y, \sigma_z, \rho)_{m,t}^i$ for an agent, mode, and timestep.

E. Loss Function

Our model is trained end-to-end using two components; (1) a *regression* component, \mathcal{L}^{nll} , which back-propagates the average negative log-likelihood between the predictions and ground truth, and (2) a *classification* component, \mathcal{L}^{ce} , which is the cross-entropy between the model's predicted confidences for each of the M prediction heads and the one-hot encoding of the predicted future with the smallest error. The total loss is expressed as, $\mathcal{L}^{total} = \lambda^{nll} \mathcal{L}^{nll} + \lambda^{ce} \mathcal{L}^{ce}$, where, $\lambda^{nll}, \lambda^{ce} \in \mathbb{R}$ are weighting hyperparameters.

VI. Implementation Details

Dataset: We consider the 10 airports introduced in Section IV.A for which we post-processed a randomly chosen month of trajectory data, representing ~ 720 hours (Table 2). To split the data into a *train/val* and *test* sets, we use a *day*-based splitting strategy where 80% of each airport’s collected days are used for training/validation and the remaining 20%, for testing. The days in each subset are chosen randomly.

Scene Representation: We split the data into $T = 60$ seconds scenes to capture long-horizon interactions, where the first $H = 10$ seconds are the historical segment and the remaining $F = 50$ seconds are for prediction to encourage long-horizon and preemptive reasoning from minimal historical information. The scene length selection was determined empirically, but as we will show in our scene visualizations, it is sufficient to capture long-horizon and diverse maneuvers.

We consider scenes containing a minimum of 2 agents and a maximum of 15. We then select a maximum of $K = 5$ agents as the *relevant* agents following the selection process described in Section V.B. We obtain each selected agent’s local context consisting of the $P = 100$ closest points to their location at the last observed timestep. Through this scheme, we obtain over **19.2M scenes**, comprising $\sim 158.2\text{M sequences}$ or **9.4B tokens**, where each token represents an agent’s state at a given timestep.

Model: We use a 5-layer MLP with layer normalization to extract agent features and a 4-layer MLP with batch normalization to extract context features. Our scene encoder is built using 3 TIC blocks. Each layer in the block consists of an MHA module with $h = 8$ attention heads and a 5-layer MLP that outputs the final feature embeddings. Finally, our GMM is built as a 2-layer MLP with a GELU activation and produces $M = 4$ output heads. The hidden dimensions of all MLPs are of size $D = 256$. The final model comprises $\sim 89.8\text{M parameters}$. We train it for at most 100 epochs and use a standard Adam optimizer with a learning rate of $lr = 1e - 4$.

Metrics: We consider commonly adopted trajectory forecasting metrics [31, 38, 52]: *Minimum Average Displacement Error* (mADE) and *Minimum Final Displacement Error* (mFDE) to assess the performance of our model. In our experiments, we show results at $F = 20$ and $F = 50$ to assess our model’s performance over a *short* and a *long* horizon.

VII. Results

We now study the performance of *Amelia-TF*. In Section VII.A, we present an analysis of the scene representation strategy introduced in Section V, and in Section IV.B, we present baseline results across our proposed benchmark.

A. Scene Representation Results

We first study whether our scene selection strategy (*Critical*) produces more complex and critical interactions by comparing it against a baseline selection approach in which K agents are randomly chosen to represent a scene (*Random*). As proxies for these components, we analyze the percentage of stationary agents selected as ego agents, as

well as the average closest distance between a given agent in a scene and the closest conflict point.

Table 4 Ego-agent selection statistics for the Random and Critical strategies. In parentheses, we show the relative percentage difference between relevant and random strategies.

Airport	Total Num. Ego-agents	Random Selection Strategy				Critical Selection Strategy			
		Stationary Ego-agents (%)	Avg. Closest Dist. to Conflict Point (m)			Stationary Ego-agents (%)	Avg. Closest Dist. to Conflict Point (m)		
			All Agents	Stationary Agents	Moving Agents		All Agents	Stationary Agents	Moving Agents
PANC	481,353	1.84	74.44	74.15	107.87	1.75 (-4.89%)	72.26 (-2.93%)	72.08 (-2.80%)	96.40 (-10.64%)
KBOS	435,162	15.28	82.30	69.43	153.66	11.30 (-26.05%)	70.44 (-14.42%)	60.44 (-12.95%)	148.96 (-3.06%)
KDCA	455,366	43.92	103.48	95.84	113.25	36.84 (-16.12%)	99.61 (-3.74%)	92.25 (-3.74%)	112.23 (-0.90%)
KEWR	195,615	10.58	95.14	92.95	113.62	7.97 (-24.67%)	83.29 (-12.45%)	81.40 (-12.43%)	105.12 (-7.49%)
KJFK	54,458	38.29	88.30	78.38	104.27	30.60 (-20.08%)	74.79 (-15.30%)	68.42 (-12.71%)	89.23 (-14.43%)
KLAX	125,602	5.26	50.55	49.24	74.04	4.27 (-18.82%)	47.01 (-6.99%)	46.52 (-5.53%)	58.15 (-21.47%)
KMDW	268,734	9.49	66.58	70.54	28.84	9.91 (4.43%)	58.14 (-12.69%)	61.93 (-12.21%)	23.69 (-17.86%)
KMSY	673,439	17.69	147.63	149.73	137.85	17.87 (1.02%)	144.20 (-2.32%)	146.11 (-2.42%)	135.41 (-1.77%)
KSEA	85,948	4.51	81.19	79.17	124.06	3.24 (-28.16%)	77.57 (-4.45%)	76.15 (-3.81%)	120.03 (-3.25%)
KSFO	186,436	26.22	82.76	78.19	95.62	20.70 (-21.05%)	68.25 (-17.54%)	65.34 (-16.44%)	79.42 (-16.95%)
Average	296,211	17.31	87.24	83.76	105.31	14.45 (-15.44%)	79.55 (-9.28%)	77.06 (-8.50%)	96.86 (-9.78%)

Note: The percentage of stationary agents and the average closest distance to a conflict point are reported for the test set.

Table 4 summarizes the per-airport ego-agent selection statistics for both strategies. Each column in **Critical**, shows in parentheses the average percentage change w.r.t. **Random**. Overall, we show that **Critical** generally selects agents with more dynamic profiles as depicted by the **15%** average reduction for the percentage of selected stationary ego agents. The table further shows that our strategy selects more agents on average **10%** closer to conflict regions.

We compare qualitative results in Figure 8. We show paired scenes for various airports depicting all agents in the scene, the (K-1)-relevant agents (orange halo), and the selected ego agent (blue halo). This figure shows that our selection strategy often selects more dynamic agents, e.g., aircraft preparing for take-off or landing, and agents in conflicting regions, e.g., aircraft vacating a taxiway. Moreover, the agent-to-agent relationships between the selected relevant agents within our strategy are generally more critical. For example, our strategy often selects aircraft that are either vacating or potentially crossing through a runway soon to be used by another aircraft preparing for take-off. In contrast, the random strategy more often selects less dynamic, non-critical agents.

B. The Amelia-10 Benchmark Results

We now study the performance of **Amelia-TF** on the **Amelia-10**. We thus report short-horizon results in Table 5 and long-horizon results in Table 6. Each column shows the mADE/mFDE results for a given airport’s test set, and the last column shows the average across all airports. For reference, the first row shows **SingleAirport** results, and each of the remaining rows represents a **MultiAirport** experiment. In **MultiAirport**, the white and gray cells represent the seen (*within-domain*) and unseen (*domain shift*) airports for the given experiment, respectively. We **bold** the best mADE/mFDE values across the experiment sweep and show in **green** the values that were lower than the results obtained in **SingleAirport**.

Overall, our experiments show that generalization across unseen airports improves significantly as we increase the variety and scale of seen environments. However, we also observe that even in more environment-constrained

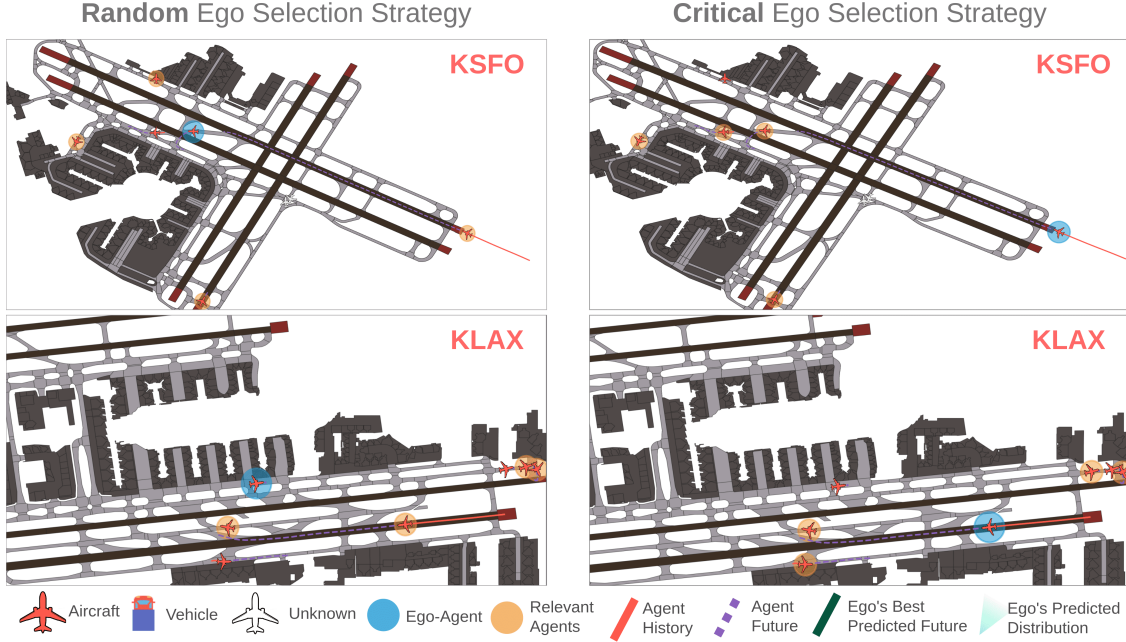


Fig. 8 Scene representation and prediction results for the Random and Critical scene representation strategies, showing that the proposed strategy generally selects agents with a more relevant kinematic and interactive profile.

experiments, our model generally exhibits strong performance. We attribute this, in part, to our scene representation strategy, which aims to abstract and prioritize scene information more effectively. Nonetheless, a gap between experiments across the sweep still remains. In the short-horizon results, we show that the 7-Seen experiment achieves the lowest average mADE/mFDE from the sweep of experiments, closing the gap to SingleAirport to +1.60%/-2.35%. Furthermore, results across all airports as well the results for KSEA, KDCA, PANC and KLAX as lower than those obtained in SingleAirport. In the long-horizon results, we show that the All-Seen experiment achieves the lowest average mADE/mFDE from the full sweep of experiments, closing the gap to SingleAirport to -4.68%/-4.83%. Here, our model achieves better results for PANC, KLAX, KJFK than in SingleAirport.

Table 5 We show **Amelia-10** results for a prediction horizon of F=20. In each row, we highlight in light gray the airports that were not included in the experiment's training set, i.e., the *unseen* airports. In the final column, we show the average mADE/mFDE across all airports. Bolded values represent the lowest mADE and mFDE across the sweep. We highlight in green values that were lower than the SingleAirport experiment. In parentheses, we show the relative change w.r.t. SingleAirport for the average over all airports. All results are shown in meters.

Experiment	KMDW mADE / mFDE	KEWR mADE / mFDE	KBOS mADE / mFDE	KSFO mADE / mFDE	KSEA mADE / mFDE	KDCA mADE / mFDE	PANC mADE / mFDE	KLAX mADE / mFDE	KMSY mADE / mFDE	KJFK mADE / mFDE	Average mADE / mFDE
Single-Airport	3.30 / 6.12	6.61 / 12.92	5.58 / 10.90	5.06 / 9.82	9.76 / 18.35	4.74 / 9.22	10.11 / 20.87	11.36 / 20.63	2.73 / 5.12	4.58 / 9.52	6.38 / 12.35
All-Seen	3.88 / 7.70	7.87 / 15.80	6.87 / 14.34	6.09 / 12.64	9.03 / 18.35	4.84 / 9.55	8.24 / 16.75	8.80 / 16.73	3.22 / 6.25	4.56 / 9.64	6.34 (+0.70%) / 12.77 (-3.35%)
7-Seen	3.59 / 7.03	7.30 / 14.54	6.59 / 13.59	5.73 / 11.65	8.30 / 16.71	4.55 / 8.82	7.48 / 14.94	9.99 / 19.35	4.64 / 9.85	4.66 / 9.96	6.28 (+1.60%) / 12.64 (-2.35%)
4-Seen	3.52 / 6.74	7.26 / 14.33	6.31 / 12.68	5.66 / 11.33	9.79 / 20.42	5.99 / 12.28	9.22 / 19.14	10.70 / 21.16	4.18 / 9.05	4.80 / 10.27	6.74 (-5.32%) / 13.74 (-10.15%)
3-Seen	3.26 / 6.59	7.25 / 14.20	6.05 / 12.11	7.25 / 15.50	9.90 / 20.95	6.16 / 12.74	9.53 / 20.26	10.99 / 21.86	4.33 / 9.29	4.96 / 10.54	6.97 (-8.74%) / 14.40 (-14.29%)
2-Seen	3.31 / 6.23	6.92 / 13.45	8.17 / 17.63	7.49 / 17.18	10.57 / 22.86	6.04 / 12.47	10.61 / 23.00	12.78 / 26.34	4.49 / 9.64	5.21 / 11.15	7.56 (-15.56%) / 15.99 (-22.81%)
1-Seen	3.30 / 6.12	13.76 / 30.91	11.30 / 25.58	9.68 / 21.73	14.07 / 31.44	7.80 / 16.07	15.00 / 33.75	15.49 / 33.13	7.43 / 17.11	7.40 / 16.77	10.52 (-39.33%) / 23.26 (-46.92%)

Finally, Figure 9 depicts qualitative examples for 7-Seen, showing *seen* (left column) and *unseen* (right column) airports. In particular, the figure shows the model's predictions on four common aircraft operations: take-off roll (first

Table 6 We show *Amelia-10* results for the *generalization* experiment for a prediction horizon of F=50.

Experiment	KMDW mADE / mFDE	KEWR mADE / mFDE	KBOS mADE / mFDE	KSFO mADE / mFDE	KSEA mADE / mFDE	KDCA mADE / mFDE	PANC mADE / mFDE	KLAX mADE / mFDE	KMSY mADE / mFDE	KJFK mADE / mFDE	Average mADE / mFDE
Single-Airport	11.50 / 28.80	23.68 / 57.63	21.34 / 53.76	17.05 / 40.23	29.94 / 65.82	16.42 / 40.57	38.84 / 101.89	36.08 / 88.25	9.89 / 25.68	17.11 / 41.19	22.18 / 54.39
All-Seen	15.30 / 40.91	28.76 / 70.23	28.52 / 73.57	22.63 / 53.78	30.41 / 68.98	17.86 / 44.88	30.19 / 72.78	29.73 / 72.46	12.31 / 33.04	17.00 / 40.92	23.27 (-4.68%) / 57.16 (-4.83%)
7-Seen	14.35 / 38.62	26.83 / 66.12	27.57 / 71.84	20.81 / 50.01	28.29 / 64.69	16.40 / 41.25	27.40 / 66.74	34.60 / 85.90	19.87 / 54.56	17.71 / 42.84	23.38 (-5.12%) / 58.26 (-6.63%)
4-Seen	12.71 / 31.64	25.54 / 59.18	23.88 / 58.45	19.78 / 46.72	33.36 / 73.86	22.40 / 54.04	35.24 / 83.90	36.42 / 85.11	17.93 / 47.47	18.58 / 43.97	24.58 (-9.76%) / 58.43 (-6.92%)
3-Seen	12.46 / 31.81	25.15 / 57.29	23.20 / 56.48	28.33 / 67.40	35.70 / 81.02	24.32 / 59.55	38.85 / 92.94	39.02 / 91.96	19.53 / 51.52	19.37 / 47.06	26.59 (-16.57%) / 63.70 (-14.61%)
2-Seen	11.84 / 29.89	24.62 / 59.04	34.89 / 88.52	31.69 / 78.28	40.37 / 96.33	24.00 / 62.72	43.30 / 107.04	48.91 / 122.31	19.29 / 51.33	20.54 / 51.20	29.94 (-25.92%) / 74.67 (-27.15%)
1-Seen	11.50 / 28.80	56.14 / 140.59	48.16 / 124.34	40.54 / 103.97	54.24 / 130.67	28.90 / 73.87	61.62 / 156.56	63.20 / 164.52	30.59 / 80.23	29.51 / 73.97	42.44 (-47.73%) / 107.75 (-49.52%)

row), landing (second), vacating a runway upon landing (third), and taxiing in preparation for take-off (fourth). Through varying airport topologies and agent distributions within the map, these results show that *Amelia-TF* is able to make strong long-term predictions for each of the tasks in both settings.

VIII. Limitations & Future Work

Scaling Up: Our largest model thus far has been trained on 10 months of data from 10 different airports. While this represents over 9.4B tokens of positional data from more than 19M scenes, we believe further scaling and model improvements are needed to cover a larger, more diverse space of airport operations and improve long-term generalization performance. To this end, we plan to continue collecting more data. However, further scaling would also require model changes to improve efficiency and performance. This work focused on representing relevant scenes via scoring and characterizing the kinematic and interactive profiles for each agent and selecting the most *relevant* ones. One promising direction, thus, is to continue exploring scene representation and encoding strategies for capturing agent-to-agent and agent-to-map relationships more effectively. Additionally, adaptation techniques could be explored to reduce performance drops both in *seen* and *unseen* airports, especially for long-horizon forecasting.

Future Applications: Predictive models for airport operations can be used for various tasks. For instance, *Amelia-TF* model can be combined with provably safe methods [17, 53] as a data-driven collision risk assessment (CRA) methodology to reduce the number of false alarms and help in mitigating near misses. To evaluate CRA methods, one avenue would be to mine the *Amelia-48* dataset for reported incidents. These examples can be used to train or test safety-critical anomaly detection methods, thereby improving the models and providing a consistent benchmarking in the aviation domain. *Amelia-TF* model can also be used downstream for improving taxi-out time predictions, departure metering and time-of-arrival calculations.

IX. Conclusions

This work contributes *Amelia-48*, a large-scale dataset for airport surface movement, which comprises trajectory information and graph-based representations of the airport maps. We validate our dataset and data processing pipelines, providing statistical analyses, visualizations, and insights for 10 major U.S. airports. To the best of our knowledge, this is the **largest dataset of its kind in the public domain**, specifically geared toward training next-generation data-driven

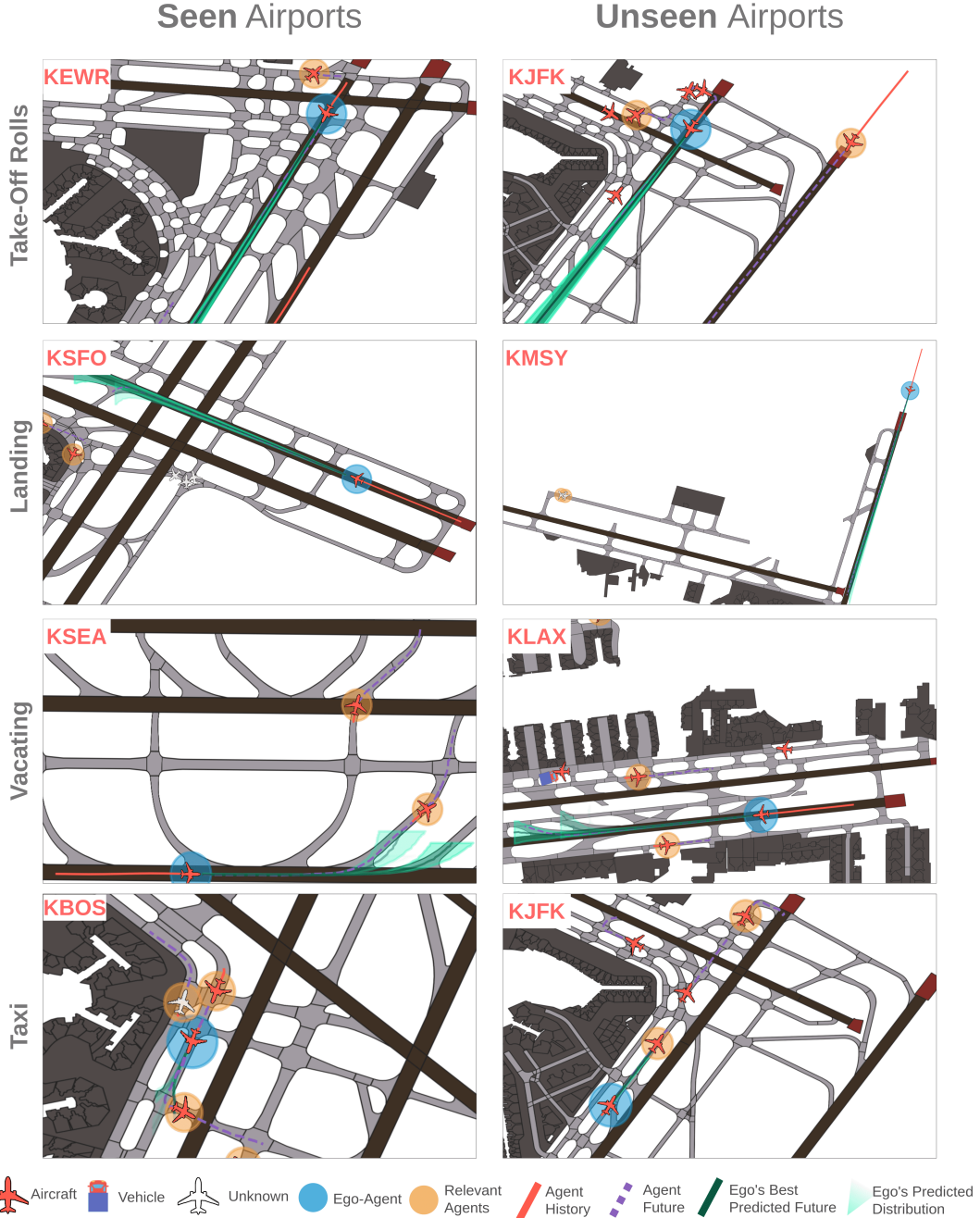


Fig. 9 Prediction results for the 7-Seen experiment on four different tasks: take-off roll, landing, vacating a runway, and taxiing. We compare long-horizon ($F = 50$ s) predictions for *seen* (left column) and *unseen* airports (right column).

predictive models for airport surface operations.

We also contribute *Amelia-TF*, a large transformer-based trajectory forecasting model trained on ~ 9.4 billion tokens of the processed dataset to showcase a downstream application for our dataset. *Amelia-TF* leverages a scene characterization methodology to capture relevant interaction modes across the dataset. Through *Amelia-10*, the

generalization qualities are investigated on held-out airports through rigorous analysis for *short-* and *long-term* prediction horizons. The results across our experiments showcase the strong performance of `Amelia-TF` across various axes of analysis, exhibiting multi-future zero-shot generalization capabilities to previously unseen airports. This is the **first multi-airport generalizable airport surface trajectory forecasting model in the public domain**. As such, we provide details on the design choices and training recipes to enable replication of results and downstream use for various subtasks. Furthermore, we invite other researchers to use the strong multi-future modeling capabilities for various applications such as collision risk assessment, anomaly detection, and taxi-out time predictions. Finally, we also **open-source all data and model tools** at: ameliacmu.github.io.

Funding Sources

This work was supported by Boeing (award #2022UIPA422). This work used Bridges-2 at Pittsburgh Supercomputing Center through allocation `cis220039p` from the Advanced Cyberinfrastructure Coordination Ecosystem: Services & Support (ACCESS) program, which is supported by National Science Foundation grants #2138259, #2138286, #2138307, #2137603, and #2138296. This work was also supported by the Korean Ministry of Trade, Industry, and Energy (MOTIE; grant #P0026022), and by the Korea Institute of Advancement of Technology (KIAT), through the International Cooperative R&D program (#P0019782): Embedded AI Based fully autonomous driving software and Maas technology development.

Acknowledgments

We thank Charles Erignac and Chad McFarland for their support and feedback throughout the project.

References

- [1] Daugherty, A., “‘We were very lucky’: Near-collisions spark new worries for air travel,” *POLITICO*, 2023.
- [2] Leussink, D., Kaneko, K., and Barrington, L., “Japan Airlines counts losses from wrecked Tokyo Plane,” *Reuters*, 2024.
- [3] Helmuth Rosales, M. G., K.K. Rebecca Lai, and Ismay, J., “What the Black Hawk Pilots Could See, Just Before the Crash,” *The New York Times*, 2025.
- [4] Ruberg, S., “1 Killed as Plane Owned by Mötley Crüe Singer Strikes Parked Jet,” *The New York Times*, 2025.
- [5] Ember, S., and Steel, E., “Airline Close Calls Happen Far More Often Than Previously Known,” *The New York Times*, 2023.
- [6] Association, I. A. T., “Air Passenger Market Analysis - December 2022,” Tech. rep., IATA, 2022.
- [7] Aratani, L., “TSA broke record on Sunday for number of passengers screened,” *The Washington Post*, 2023.

[8] Degas, A., Islam, M. R., Hurter, C., Barua, S., Rahman, H., Poudel, M., Ruscio, D., Ahmed, M. U., Begum, S., Rahman, M. A., et al., “A survey on artificial intelligence (ai) and explainable ai in air traffic management: Current trends and development with future research trajectory,” *Applied Sciences*, Vol. 12, No. 3, 2022, p. 1295.

[9] Sun, P., Kretzschmar, H., Dotiwalla, X., Chouard, A., Patnaik, V., Tsui, P., Guo, J., Zhou, Y., Chai, Y., Caine, B., et al., “Scalability in perception for autonomous driving: Waymo open dataset,” *Proceedings of the IEEE/CVF conference on computer vision and pattern recognition*, 2020, pp. 2446–2454.

[10] Chang, M., Lambert, J., Sangkloy, P., Singh, J., Bak, S., Hartnett, A., Wang, D., Carr, P., Lucey, S., Ramanan, D., and Hays, J., “Argoverse: 3D Tracking and Forecasting With Rich Maps,” *IEEE Conference on Computer Vision and Pattern Recognition, CVPR 2019, Long Beach, CA, USA, June 16-20, 2019*, Computer Vision Foundation / IEEE, 2019, pp. 8748–8757. <https://doi.org/10.1109/CVPR.2019.00895>.

[11] Caesar, H., Bankiti, V., Lang, A. H., Vora, S., Lioung, V. E., Xu, Q., Krishnan, A., Pan, Y., Baldan, G., and Beijbom, O., “nuscenes: A multimodal dataset for autonomous driving,” *Proceedings of the IEEE/CVF conference on computer vision and pattern recognition*, 2020, pp. 11621–11631.

[12] Rudenko, A., Palmieri, L., Herman, M., Kitani, K. M., Gavrila, D. M., and Arras, K. O., “Human motion trajectory prediction: a survey,” *Int. J. Robotics Res.*, Vol. 39, No. 8, 2020. <https://doi.org/10.1177/0278364920917446>.

[13] Pellegrini, S., Ess, A., Schindler, K., and Gool, L. V., “You’ll never walk alone: Modeling social behavior for multi-target tracking,” *IEEE 12th International Conference on Computer Vision, ICCV 2009, Kyoto, Japan, September 27 - October 4, 2009*, IEEE Computer Society, 2009, pp. 261–268. <https://doi.org/10.1109/ICCV.2009.5459260>.

[14] Lerner, A., Chrysanthou, Y., and Lischinski, D., “Crowds by Example,” *Comput. Graph. Forum*, Vol. 26, No. 3, 2007, pp. 655–664. <https://doi.org/10.1111/j.1467-8659.2007.01089.x>.

[15] Navarro, I., Patrikar, J., Dantas, J. P. A., Baijal, R., Higgins, I., Scherer, S., and Oh, J., “SoRTS: Learned Tree Search for Long Horizon Social Robot Navigation,” *IEEE Robotics and Automation Letters*, Vol. 9, No. 4, 2024, pp. 3759–3766. <https://doi.org/10.1109/LRA.2024.3370051>.

[16] Patrikar, J., Dantas, J., Ghosh, S., Kapoor, P., Higgins, I., Aloor, J. J., Navarro, I., Sun, J., Stoler, B., Hamidi, M., et al., “Challenges in close-proximity safe and seamless operation of manned and unmanned aircraft in shared airspace,” *arXiv preprint arXiv:2211.06932*, 2022.

[17] Muthali, A., Shen, H., Deglurkar, S., Lim, M. H., Roelofs, R., Faust, A., and Tomlin, C., “Multi-agent reachability calibration with conformal prediction,” *arXiv preprint arXiv:2304.00432*, 2023.

[18] Sui, D., Chen, H., and Zhou, T., “A Conflict Resolution Strategy at a Taxiway Intersection by Combining a Monte Carlo Tree Search with Prior Knowledge,” *Aerospace*, Vol. 10, No. 11, 2023, p. 914.

[19] Kong, Y., and Mahadevan, S., “Identifying Anomalous Behavior in Aircraft Landing Trajectory Using a Bayesian Autoencoder,” *Journal of Aerospace Information Systems*, 2023, pp. 1–9.

[20] Memarzadeh, M., Matthews, B. L., and Weckler, D. I., “Anomaly Detection in Flight Operational Data Using Deep Learning,” *System-Wide Safety Technical Challenge 1 Close Out Event*, 2023.

[21] Liu, Y., Hansen, M., Gupta, G., Malik, W., and Jung, Y., “Predictability impacts of airport surface automation,” *Transportation Research Part C: Emerging Technologies*, Vol. 44, 2014, pp. 128–145.

[22] Lee, H., Malik, W., and Jung, Y. C., “Taxi-out time prediction for departures at Charlotte airport using machine learning techniques,” *16th AIAA Aviation Technology, Integration, and Operations Conference*, 2016, p. 3910.

[23] Wang, F., Bi, J., Xie, D., and Zhao, X., “A data-driven prediction model for aircraft taxi time by considering time series about gate and real-time factors,” *Transportmetrica A: Transport Science*, Vol. 19, No. 3, 2023, p. 2071353.

[24] Alsalous, O., and Hotle, S., “Deicing Facility Capacity and Delay Estimation Using ASDE-X Data: Chicago O’Hare Simulation Case Study,” *Transportation Research Record*, 2023, p. 03611981231185147.

[25] Gui, X., Zhang, J., Peng, Z., and Yang, C., “Data-driven method for the prediction of estimated time of arrival,” *Transportation Research Record*, Vol. 2675, No. 12, 2021, pp. 1291–1305.

[26] Li, M. Z., and Ryerson, M. S., “Reviewing the DATAS of aviation research data: Diversity, availability, tractability, applicability, and sources,” *Journal of Air Transport Management*, Vol. 75, 2019, pp. 111–130.

[27] Zhang, X., Zhong, S., and Mahadevan, S., “Airport surface movement prediction and safety assessment with spatial–temporal graph convolutional neural network,” *Transportation research part C: emerging technologies*, Vol. 144, 2022, p. 103873.

[28] Park, D. K., and Kim, J. K., “Influential factors to aircraft taxi time in airport,” *Journal of Air Transport Management*, Vol. 106, 2023, p. 102321.

[29] Ranson, L., “FAA completes roll-out of ASDE-X anti-incursion surveillance,” *Flight International*, Vol. 180, No. 5313, 2011, pp. 15–15.

[30] Vaswani, A., Shazeer, N., Parmar, N., Uszkoreit, J., Jones, L., Gomez, A. N., Kaiser, Ł., and Polosukhin, I., “Attention is all you need,” *Advances in neural information processing systems*, Vol. 30, 2017.

[31] Patrikar, J., Moon, B., Oh, J., and Scherer, S., “Predicting like a pilot: Dataset and method to predict socially-aware aircraft trajectories in non-towered terminal airspace,” *2022 International Conference on Robotics and Automation (ICRA)*, IEEE, 2022, pp. 2525–2531.

[32] Gao, J., Sun, C., Zhao, H., Shen, Y., Anguelov, D., Li, C., and Schmid, C., “Vectornet: Encoding hd maps and agent dynamics from vectorized representation,” *Proceedings of the IEEE/CVF Conference on Computer Vision and Pattern Recognition*, 2020, pp. 11525–11533.

[33] Nayakanti, N., Al-Rfou, R., Zhou, A., Goel, K., Refaat, K. S., and Sapp, B., “Wayformer: Motion forecasting via simple & efficient attention networks,” *2023 IEEE International Conference on Robotics and Automation (ICRA)*, IEEE, 2023, pp. 2980–2987.

[34] Cui, A., Casas, S., Wong, K., Suo, S., and Urtasun, R., “Gorela: Go relative for viewpoint-invariant motion forecasting,” *2023 IEEE International Conference on Robotics and Automation (ICRA)*, IEEE, 2023, pp. 7801–7807.

[35] Shi, S., Jiang, L., Dai, D., and Schiele, B., “Motion transformer with global intention localization and local movement refinement,” *Advances in Neural Information Processing Systems*, Vol. 35, 2022, pp. 6531–6543.

[36] Yuan, Y., Weng, X., Ou, Y., and Kitani, K. M., “Agentformer: Agent-aware transformers for socio-temporal multi-agent forecasting,” *Proceedings of the IEEE/CVF International Conference on Computer Vision*, 2021, pp. 9813–9823.

[37] Ngiam, J., Vasudevan, V., Caine, B., Zhang, Z., Chiang, H.-T. L., Ling, J., Roelofs, R., Bewley, A., Liu, C., Venugopal, A., et al., “Scene transformer: A unified architecture for predicting future trajectories of multiple agents,” *International Conference on Learning Representations*, 2021, pp. 541–556.

[38] Navarro, I., and Oh, J., “Social-PatteRNN: Socially-Aware Trajectory Prediction Guided by Motion Patterns,” *2022 IEEE/RSJ International Conference on Intelligent Robots and Systems (IROS)*, IEEE, 2022, pp. 9859–9864.

[39] Alahi, A., Goel, K., Ramanathan, V., Robicquet, A., Fei-Fei, L., and Savarese, S., “Social lstm: Human trajectory prediction in crowded spaces,” *Proceedings of the IEEE conference on computer vision and pattern recognition*, 2016, pp. 961–971.

[40] Zhao, D., and Oh, J., “Noticing motion patterns: A temporal cnn with a novel convolution operator for human trajectory prediction,” *IEEE Robotics and Automation Letters*, Vol. 6, No. 2, 2020, pp. 628–634.

[41] Stoler, B., Navarro, I., Jana, M., Hwang, S., Francis, J., and Oh, J., “SafeShift: Safety-Informed Distribution Shifts for Robust Trajectory Prediction in Autonomous Driving,” *2024 IEEE Intelligent Vehicles Symposium (IV)*, 2024, pp. 1179–1186. <https://doi.org/10.1109/IV55156.2024.10588828>.

[42] Guo, D., Wu, E. Q., Wu, Y., Zhang, J., Law, R., and Lin, Y., “FlightBERT: Binary Encoding Representation for Flight Trajectory Prediction,” *IEEE Transactions on Intelligent Transportation Systems*, Vol. 24, No. 2, 2023, pp. 1828–1842. <https://doi.org/10.1109/TITS.2022.3219923>, URL <https://ieeexplore.ieee.org/document/9945661>, conference Name: IEEE Transactions on Intelligent Transportation Systems.

[43] Guo, D., Zhang, Z., Yan, Z., Zhang, J., and Lin, Y., “FlightBERT++: A Non-autoregressive Multi-Horizon Flight Trajectory Prediction Framework,” *Proceedings of the AAAI Conference on Artificial Intelligence*, Vol. 38, No. 1, 2024, pp. 127–134. <https://doi.org/10.1609/aaai.v38i1.27763>, URL <https://ojs.aaai.org/index.php/AAAI/article/view/27763>, number: 1.

[44] Zhang, Z., Guo, D., Zhou, S., Zhang, J., and Lin, Y., “Flight trajectory prediction enabled by time-frequency wavelet transform,” *Nature Communications*, Vol. 14, No. 1, 2023, p. 5258. <https://doi.org/10.1038/s41467-023-40903-9>, URL <https://www.nature.com/articles/s41467-023-40903-9>, publisher: Nature Publishing Group.

[45] Yin, Y., Zhang, S., Zhang, Y., Zhang, Y., and Xiang, S., “Context-aware Aircraft Trajectory Prediction with Diffusion Models,” *2023 IEEE 26th International Conference on Intelligent Transportation Systems (ITSC)*, IEEE, 2023, pp. 5312–5317.

[46] Robb, J., “System wide information management (SWIM): program overview and status update,” *2014 Integrated Communications, Navigation and Surveillance Conference (ICNS) Conference Proceedings*, IEEE, 2014, pp. 1–15.

[47] Vinoski, S., “Advanced message queuing protocol,” *IEEE Internet Computing*, Vol. 10, No. 6, 2006, pp. 87–89.

[48] Map, O. S., “Open street map,” *Online: <https://www.openstreetmap.org>. Search in*, 2014.

[49] Boeing, G., “OSMnx: New methods for acquiring, constructing, analyzing, and visualizing complex street networks,” *Computers, Environment and Urban Systems*, Vol. 65, 2017, pp. 126–139.

[50] Melnychuk, V., Frauen, D., and Feuerriegel, S., “Causal transformer for estimating counterfactual outcomes,” *International Conference on Machine Learning*, PMLR, 2022, pp. 15293–15329.

[51] Ho, J., Kalchbrenner, N., Weissenborn, D., and Salimans, T., “Axial attention in multidimensional transformers,” *arXiv preprint arXiv:1912.12180*, 2019.

[52] Chai, Y., Sapp, B., Bansal, M., and Anguelov, D., “Multipath: Multiple probabilistic anchor trajectory hypotheses for behavior prediction,” *arXiv preprint arXiv:1910.05449*, 2019.

[53] Nakamura, K., and Bansal, S., “Online update of safety assurances using confidence-based predictions,” *2023 IEEE International Conference on Robotics and Automation (ICRA)*, IEEE, 2023, pp. 12765–12771.